Journal of Physics: Conference Series **454** (2013) 012002 doi:10.1088/1742-6596/454/1/012002

BSSN equations in spherical coordinates without regularization: spherically symmetric spacetimes

Pedro J Montero and Isabel Cordero-Carrión

Max-Planck-Institute für Astrophysik, Karl-Schwarzschild-Str. 1, D-85748, Garching bei München, Germany

E-mail: montero@mpa-garching.mpg.de

Abstract. Brown recently introduced a covariant formulation of the BSSN equations which is well suited for curvilinear coordinate systems. This is particularly desirable as many astrophysical phenomena are symmetric with respect to the rotation axis or are such that curvilinear coordinates adapt better to their geometry. We show results from a newly developed numerical code solving the BSSN equations in spherical symmetry and the general relativistic hydrodynamic equations written in flux-conservative form. A key feature of the code is that uses a second-order partially implicit Runge-Kutta method to integrate the evolution equations, and does not need a regularization algorithm at the origin. We discuss a number of tests to assess the accuracy, numerical stability and expected convergence of the code.

1. Introduction

The 3+1 formulation of Einstein equations originally proposed by Nakamura [1] and subsequently modified by Shibata-Nakamura [2] and Baumgarte-Shapiro [3], which is usually known as the BSSN formulation, has become the most widespread used formulation in the numerical relativity community. The main drawback of the BSSN formulation in its original form resides in the fact that it is particularly tuned for Cartesian coordinates, since this involves dynamical fields which are not true tensors and assumes that the determinant of the conformal metric is equal to one. Brown [4] addressed this issue and introduced a covariant formulation of the BSSN equations which is well suited for curvilinear coordinate systems.

However, the singularities associated with the curvilinear coordinate systems are a known source of numerical problems. For instance, one problem arises because of the presence of terms in the evolution equations that behave like $1/r$ near the origin $r = 0$. Although on the analytical level the regularity of the metric ensures that these terms cancel exactly, on the numerical level this is not necessarily the case, and special care should be taken in order to avoid numerical instabilities. A similar problem appears also near the axis of symmetry in axisymmetric systems if curvilinear coordinate are used.

Several methods have been proposed to handle the issue of regularity in curvilinear coordinates. One possible approach is to apply a regularization procedure. One such regularization method, presented by [5], enforces both the appropriate parity regularity conditions and local flatness in order to achieve the desired regularity of the evolution equations. Such method has the advantage that it allows a more generic gauge choice, and has been explored by [6, 7, 8] who have performed several numerical simulations of regular spacetimes in spherical

Content from this work may be used under the terms of the Creative Commons Attribution 3.0 licence. Any further distribution of this work must maintain attribution to the author(s) and the title of the work, journal citation and DOI.
Published under licence by IOP Publishing Ltd

and axial symmetry. A disadvantage of such a regularization algorithm is that it is not easy to implement numerically both conditions simultaneously, and it requires the introduction of auxiliary variables as well as finding their evolution equations. This is an obstacle if one wants to perform 3D simulations of regular spacetimes with spherical coordinates.

Implicit or partially implicit methods are used to deal with systems of equations that require a special numerical treatment in order to achieve stable evolutions. The origin of the numerical instabilities may be diverse. Stiff source terms in the equations can lead to the development of numerical instabilities, and with some choices of the coordinate system, source terms may introduce factors which can be numerically interpreted as stiff terms (e.g., $1/r$ factors due to spherical coordinates close to $r = 0$ even when regular data is evolved).

Recently, partially implicit Runge-Kutta (PIRK) methods for wave-like equations in spherical coordinates [9] have been successfully applied [10] to the hyperbolic part of Einstein equations in the Fully Constrained Formulation [11]. Following this success, Montero & Cordero-Carrión [12], assuming spherical symmetry, applied a second-order PIRK method to the full set of the BSSN Einstein equations in curvilinear coordinates, and produced the first successful numerical simulations of vacuum and non-vacuum spacetimes using the covariant BSSN formulation in spherical coordinates without the need for a regularization algorithm at the origin. We discuss this approach and show a number of tests to assess the accuracy, numerical stability and expected convergence of the code; while we refer to Montero & Cordero-Carrión [12] for further details. We use units in which $c = G = M_\odot = 1$.

2. Basic equations

2.1. BSSN equations in spherical symmetry

We solve the BSSN equations in the special case of spherical symmetry [8, 12]. In particular, we follow [8] for the description of the BSSN equations below, and refer to this work for more details. Under this symmetry condition the spatial line element is written as

$$dl^2 = e^{4\chi}[a(r,t)dr^2 + r^2 b(r,t)d\Omega^2], \tag{1}$$

where $d\Omega^2$ is the solid angle element $d\Omega^2 = d\theta^2 + \sin^2\theta d\varphi^2$, $a(r,t)$ and $b(r,t)$ are the metric functions, and χ is the conformal factor defined as

$$\chi = \frac{1}{12}\ln(\gamma/\hat{\gamma}), \tag{2}$$

where $\hat{\gamma}$ is the determinant of the conformal metric. The conformal metric relates to the physical one by

$$\hat{\gamma}_{ij} = e^{-4\chi}\gamma_{ij}. \tag{3}$$

Initially, the determinant of the conformal metric fulfills the condition that it equals the determinant of the flat metric in spherical coordinates $\mathring{\gamma}_{ij}$ (i.e. $\hat{\gamma}(t=0) = \mathring{\gamma} = r^4 sin^2\theta$). Moreover, we follow the so called "Lagrangian" condition $\partial_t\hat{\gamma} = 0$ (i.e. choosing $\sigma = 1$). The evolution equation for the conformal factor $X \equiv e^{-2\chi}$ takes the form

$$\partial_t X = \beta^r\partial_r X - \frac{1}{3}X(\alpha K - \sigma\hat{\nabla}_m\beta^m), \tag{4}$$

K being the trace of the extrinsic curvature, α the lapse function, and $\hat{\nabla}_m\beta^m$ the conformal divergence of the shift vector β^i. The evolution equations for the conformal metric components are:

$$\partial_t a = \beta^r\partial_r a + 2a\partial_r\beta^r - \frac{2}{3}\sigma a\hat{\nabla}_m\beta^m - 2\alpha a A_a, \tag{5}$$

$$\partial_t b = \beta^r \partial_r b + 2b\frac{\beta^r}{r} - \frac{2}{3}\sigma b \hat{\nabla}_m \beta^m - 2\alpha b A_b, \tag{6}$$

where $\hat{A}_{ij}$ is the traceless part of the conformal extrinsic curvature, and

$$A_a \equiv \hat{A}^r_r\ , \qquad A_b \equiv \hat{A}^\theta_\theta. \tag{7}$$

Next, the evolution equation for the independent component of the traceless part of the conformal extrinsic curvature, A_a, is given by

$$\begin{aligned}\partial_t A_a = \beta^r \partial_r A_a - \left(\nabla^r \nabla_r \alpha - \frac{1}{3}\nabla^2 \alpha\right) + \alpha\left(R^r_r - \frac{1}{3}R\right) \\ + \alpha K A_a - 16\pi\alpha(S_a - S_b),\end{aligned} \tag{8}$$

where R^r_r is the mixed radial component of the Ricci tensor, R its trace. The evolution equation for K is:

$$\partial_t K = \beta^r \partial_r K - \nabla^2 \alpha + \alpha(A_a^2 + 2A_b^2 + \frac{1}{3}K^2) + 4\pi\alpha(E + S_a + 2S_b), \tag{9}$$

with the matter source terms measured by the Eulerian observers given by

$$\begin{aligned} E &= n_\mu n_\nu T^{\mu\nu}, \\ j_i &= -\gamma_{i\mu} n_\nu T^{\mu\nu}, \\ S_{ij} &= \gamma_{i\mu}\gamma_{j\nu} T^{\mu\nu}, \end{aligned} \tag{10}$$

$T^{\mu\nu}$ being the stress-energy tensor for a perfect fluid, which is written as a function of the rest-mass density ρ, the specific enthalpy h, the pressure P and the fluid 4-velocity u^μ

Finally, the evolution equation for $\hat{\Delta}^r$, the radial component of the additional BSSN variables $\hat{\Delta}^i = \hat{\gamma}^{mn}\hat{\Delta}^i_{mn}$ with $\hat{\Delta}^a_{bc} = \hat{\Gamma}^a_{bc} - \mathring{\Gamma}^a_{bc}$, is given by

$$\begin{aligned}\partial_t \hat{\Delta}^r = \beta^r \partial_r \hat{\Delta}^r - \hat{\Delta}^r \partial_r \beta^r + \frac{1}{a}\partial_r^2 \beta^r + \frac{2}{b}\partial_r\left(\frac{\beta^r}{r}\right) \\ + \frac{\sigma}{3}\left(\frac{1}{a}\partial_r(\hat{\nabla}_m \beta^m) + 2\hat{\Delta}^r \hat{\nabla}_m \beta^m\right) - \frac{2}{a}(A_a \partial_r \alpha + \alpha \partial_r A_a) \\ + 2\alpha\left(A_a \hat{\Delta}^r - \frac{2}{rb}(A_a - A_b)\right) + \frac{2\alpha}{a}\left[\partial_r A_a - \frac{2}{3}\partial_r K + 6A_a \partial_r \chi\right. \\ \left. + (A_a - A_b)\left(\frac{2}{r} + \frac{\partial_r b}{b}\right) - 8\pi j_r\right].\end{aligned} \tag{11}$$

We use the so called "non-advective 1+log" condition [13] for the lapse, and a variation of the "Gamma-driver" condition for the shift vector which has a proper vector on the right hand side[14, 8]. We do not find necessary to add a damping term on the right hand side of the shift condition in order to avoid strong oscillations of the shift vector(*i.e.* see left panel of Fig.2). These are written as follows

$$\partial_t \alpha = -2\alpha K, \tag{12}$$

$$\partial_t B^r = \frac{3}{4}\partial_t \hat{\Delta}^r, \tag{13}$$

$$\partial_t \beta^r = B^r. \tag{14}$$

The Hamiltonian constraint is used as diagnostics of the accuracy of the numerical evolutions:

$$\mathcal{H} \equiv R - (A_a^2 + 2A_b^2) + \frac{2}{3}K^2 - 16\pi E = 0. \tag{15}$$

2.2. Formulation of the hydrodynamic equations

The general relativistic hydrodynamic equations, expressed through the conservation equations for the stress-energy tensor $T^{\mu\nu}$ and the continuity equation are:

$$\nabla_\mu T^{\mu\nu} = 0\,, \qquad \nabla_\mu \left(\rho u^\mu\right) = 0. \tag{16}$$

Following [15], the general relativistic hydrodynamic equations are written in a conservative form in spherical coordinates. The following definitions for the hydrodynamic variables are used:

$$v^r \equiv \frac{u^r}{\alpha u^t} + \frac{\beta^r}{\alpha}, \tag{17}$$

$$W \equiv \alpha u^t, \tag{18}$$

where W is the Lorentz factor. By defining the vector of unknowns, $\mathbf{U}$, as

$$\mathbf{U} = \sqrt{\gamma}(D, S_r, \tau), \tag{19}$$

where the conserved quantities are D, S_r, τ. Then, the set of hydrodynamic equations (16) can be written in conservative form as

$$\partial_t \mathbf{U} + \partial_r \mathbf{F}^r = \mathbf{S}, \tag{20}$$

where $\mathbf{S}$ is the vector of sources and $\mathbf{F}^r$ the fluxes.

To close the system of equations, we choose the Γ-law equation of state, $P = (\Gamma - 1)\,\rho\epsilon$, where ϵ is the specific internal energy.

3. PIRK methods

Let us consider the following system of PDEs,

$$\begin{cases} u_t = \mathcal{L}_1(u, v), \\ v_t = \mathcal{L}_2(u) + \mathcal{L}_3(u, v), \end{cases} \tag{21}$$

$\mathcal{L}_1$, $\mathcal{L}_2$ and $\mathcal{L}_3$ being general non-linear differential operators. Let us denote by L_1, L_2 and L_3 their discrete operators, respectively. L_1 and L_3 will be treated in an explicit way, whereas the L_2 operator will be considered to contain the unstable terms and, therefore, treated partially implicitly.

We use a Runge-Kutta (RK) method to update in time the previous system (21). Each stage of the method consists of two steps: i) the variable u is evolved explicitly; ii) the variable v is evolved taking into account the updated value of u. This strategy implies that the computational costs of the methods are comparable to those of the explicit ones. The resulting numerical schemes do not need any analytical or numerical inversion, but they are able to provide stable evolutions due to their partially implicit component.

PIRK methods are described in [9] and have been derived up to third-order in Δt in such a way that the number of stages is minimized. These methods are based on stability properties for both the explicit and implicit parts, recovering the optimal SSP explicit RK methods [16] when the L_2 operator is neglected, i.e., partially implicitly treated parts are not taken into account. The second-order PIRK scheme which we use is:

$$\begin{cases} u^{(1)} = u^n + \Delta t\, L_1(u^n, v^n), \\ v^{(1)} = v^n + \Delta t \left[\dfrac{1}{2} L_2(u^n) + \dfrac{1}{2} L_2(u^{(1)}) + L_3(u^n, v^n)\right], \end{cases} \tag{22}$$

$$\begin{cases} u^{n+1} = \frac{1}{2}\left[u^n + u^{(1)} + \Delta t\, L_1(u^{(1)}, v^{(1)})\right], \\ v^{n+1} = v^n + \frac{\Delta t}{2}\left[L_2(u^n) + L_2(u^{n+1}) \right. \\ \qquad\qquad \left. + L_3(u^n, v^n) + L_3(u^{(1)}, v^{(1)})\right], \end{cases} \tag{23}$$

where Δt denotes the time-step.

This scheme is applied to the hydrodynamic and BSSN evolution equations. We include all the problematic terms appearing in the sources of the equations in the L_2 operator. Firstly, the hydrodynamic conserved quantities, the conformal metric components, a and b, the conformal factor, χ, or the quantity X (function of the conformal factor), the lapse function, α, and the radial component of the shift, β^r, are evolved explicitly (as u is evolved in the previous PIRK scheme); secondly, the traceless part of the extrinsic curvature, A_a, and the trace of the extrinsic curvature, K, are evolved partially implicitly, using explicit and implicit values of α, a and b; then, the quantity $\hat{\Delta}^r$ is evolved partially implicitly, using the updated values of α, a, b, β^r, conformal factor, A_a and K; finally, B^r is evolved partially implicitly, using the updated values of $\hat{\Delta}^r$. Matter source terms are always included in the explicitly treated parts.

4. Numerics

Derivatives in the spacetime evolution equations are calculated using a fourth-order centered finite difference approximation in a uniform grid except for the advection terms (terms formally like $\beta^r \partial_r u$), for which an upwind scheme is used. We also use fourth-order Kreiss-Oliger dissipation [17] to avoid high frequency noise appearing near the outer boundary.

We use a second-order slope limiter reconstruction scheme (MC limiter) to obtain the left and right states of the primitive variables at each cell interface, and a HLLE approximate Riemann solver [18, 19].

The computational domain is defined as $0 \leq r \leq L$, where L refers to the location of the outer boundary. We used a cell-centered grid to avoid that the location of the puncture at the origin coincides with a grid point in simulations involving a BH. At the origin we impose the conditions derived from the assumption of spherical symmetry. At the outer boundary we impose radiative boundary conditions [14] for the spacetime variables.

5. Numerical Results

5.1. Pure gauge dynamics

We first consider the propagation of a pure gauge pulse using the same initial parameters as in [8]. The main difference with respect to [8] is that we do not regularize the origin and rely only on the PIRK scheme to achieve a stable numerical simulation. The initial data are given by

$$\chi = 0, \tag{24}$$

$$a = b = 1, \tag{25}$$

$$A_a = A_b = K = 0, \tag{26}$$

$$\hat{\Delta}^r = 0, \tag{27}$$

$$\alpha = 1 + \frac{\alpha_0 r^2}{1 + r^2}\left[e^{-(r-r_0)^2} + e^{-(r+r_0)^2}\right], \tag{28}$$

with $\alpha_0 = 0.01$ and $r_0 = 5$. We evolve these initial data with a grid resolution of $\Delta r = 0.1$ and $\Delta t = 0.5\Delta r$. We use zero shift and harmonic slicing,

$$\partial_t \alpha = -\alpha^2 K. \tag{29}$$

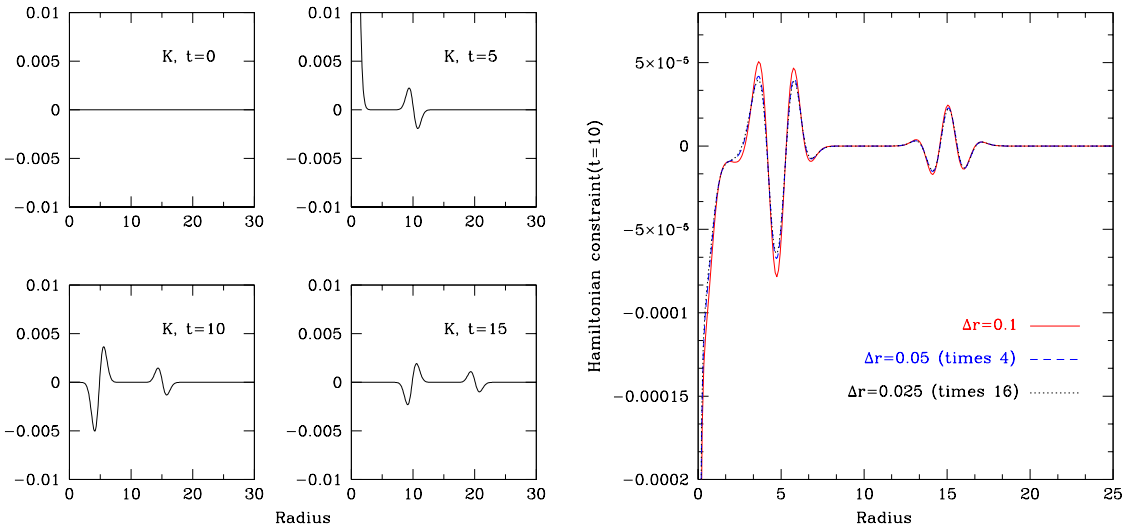

Figure 1. Left panel shows the trace of the extrinsic curvature, K, for a pure gauge pulse as a function of the radius at four different times; while in the right panel we show the Hamiltonian constraint at $t = 10$ for simulations of a pure gauge wave with three different resolutions $\Delta r = 0.1$, $\Delta r = 0.05$, and $\Delta r = 0.025$ rescaled by the factors corresponding to second-order convergence.

In the left panel of Fig. 1, we show the trace of the extrinsic curvature, K, as a function of the radius at four different times ($t = 0, 5, 10, 15$). The initial pulse separates in two pulses propagating in opposite directions. The snapshots of the evolution of the trace of the extrinsic curvature show that the evolution remains well behaved everywhere in the computational grid. We note that at $t = 5$ the value of K reaches a value of 0.1 at the origin, but later returns to zero when the pulse moves outwards as shown by [8].

In order to asses the convergence of the code, we have performed three simulations with resolutions $\Delta r = 0.1$, $\Delta r = 0.05$ and $\Delta r = 0.025$. The Hamiltonian constraint violations rescaled by the factors corresponding to second order convergence at $t = 10$ are plotted in the right panel of Fig. 1. All three lines overlap indicating that the code achieves the second-order convergence expected for the PIRK scheme used.

5.2. Schwarzschild black hole

The Schwarzschild metric in isotropic coordinates is used as initial data to test the ability of the code to evolve BH spacetimes within the moving puncture approach. The initial data are such that the 3-metric is written as

$$dl^2 = \psi^4(dr^2 + r^2 d\Omega^2), \tag{30}$$

where the conformal factor is $\psi = (1 + M/2r)$, M being the mass of the BH, which we set as $M = 1$. Here r is the isotropic radius. Initially the extrinsic curvature is $K_{ij} = 0$.

We evolve the single stationary puncture initial data with a precollapsed lapse and initially vanishing shift vector. We use the gauge conditions given by (12)–(14), with a resolution $\Delta r = 0.05$, $\Delta t = 0.5\Delta r$ and $N_r = 30000$ grid points to place the outer boundary sufficiently far way from the puncture so that errors from the boundary do not affect the evolution.

As pointed out by [20, 21], the numerical slices of a Schwarzschild BH spacetime with these gauge conditions reach a stationary state after $t \sim 20$. This is shown in Fig. 2, where the time

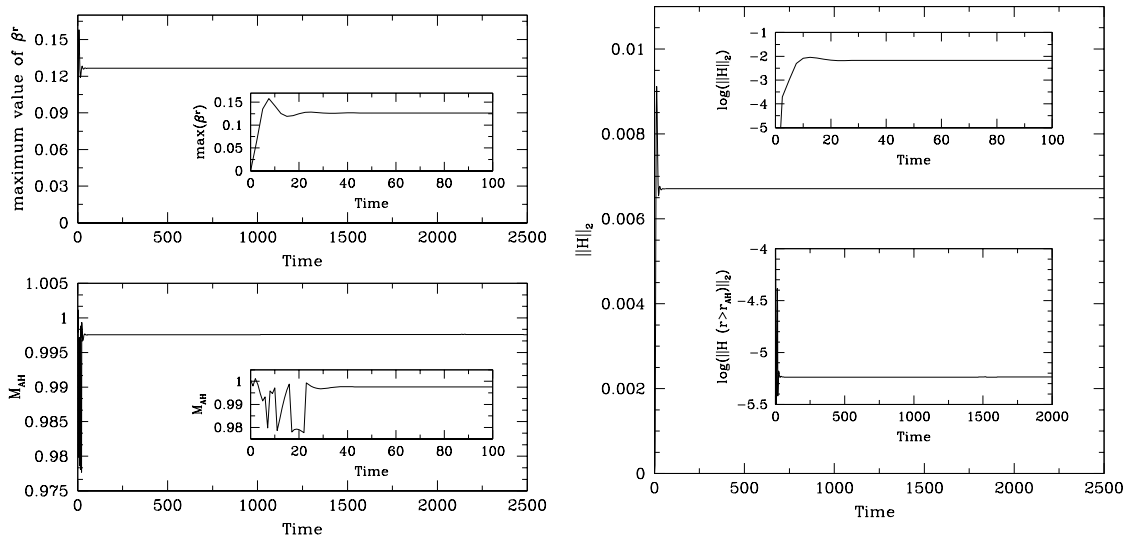

Figure 2. Left panel displays the time evolution of the maximum value of the radial shift β^r (top panel), and of the mass of the AH (bottom panel) in the single puncture BH simulation. In the right panel, we show the L2-norm of the Hamiltonian constraint in the single puncture BH simulation. The insets show the L2-norm during the initial phase, and the L2-norm computed outside the AH respectively.

evolution of the maximum value of the radial shift β^r is displayed in the upper left panel. After an initial phase in which the maximum value of the shift vector grows rapidly, it settles to a value of ~ 0.15 and we find almost no drift until the end of the simulation at $t = 2500$. In the lower left panel of Fig. 2, we show the time evolution of the mass of the apparent horizon (AH), defined as $M_{\rm AH} = \sqrt{\mathcal{A}/16\pi}$, where $\mathcal{A}$ is the area of the AH. We notice that $M_{\rm AH}$ is conserved well during the evolution and the error at $t = 2500$ is less than 0.2%

The Hamiltonian constraint violation results are displayed in the right panel of Fig. 2, which shows the L2-norm of the Hamiltonian constraint as a function of time. Both the initial phase driven by the gauge dynamics (see upper inset in the right panel of Fig. 2) and the stationary phase are clearly visible. The lower inset shows that the L2-norm computed outside the AH is about three orders of magnitude smaller than the L2-norm computed in the whole grid, which is to be expected as the largest spatial violation of the constraint occurs near the puncture (due to the finite differencing of the irregular solution).

In Fig. 3, we show the Hamiltonian constraint at $t = 100$ for simulations of single initial data with three different resolutions $\Delta r = 0.1$, $\Delta r = 0.05$, and $\Delta r = 0.025$ rescaled by the factors corresponding to second-order convergence. We find that the second-order errors associated with our PIRK method are smaller than the fourth-order error of our spatial derivatives.

5.3. Spherical relativistic stars

For our first numerical simulation of the coupling of Einstein equations and the general relativistic hydrodynamic equations, we use the Tolman-Oppenheimer-Volkoff (TOV) solution. We focus on an initial TOV model that has been extensively investigated numerically by [22, 23]. This model is a relativistic star with polytropic index $N = 1$, polytropic constant $\kappa = 100$ and central rest-mass density $\rho_c = 1.28 \times 10^{-3}$, so that its gravitational mass is $M = 1.4$, its baryon rest-mass $M_* = 1.5$ and its radius $R = 9.59$.

We evolve these initial data with our non-linear code until $t = 3000$ ($\sim$17 ms). In the upper

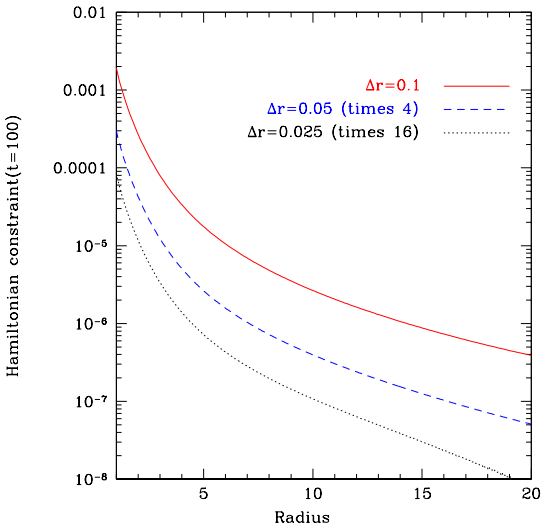

Figure 3. Hamiltonian constraint at $t = 100$ for simulations of single BH initial data with three different resolutions $\Delta r = 0.1$, $\Delta r = 0.05$, and $\Delta r = 0.025$ rescaled by the factors corresponding to second-order convergence.

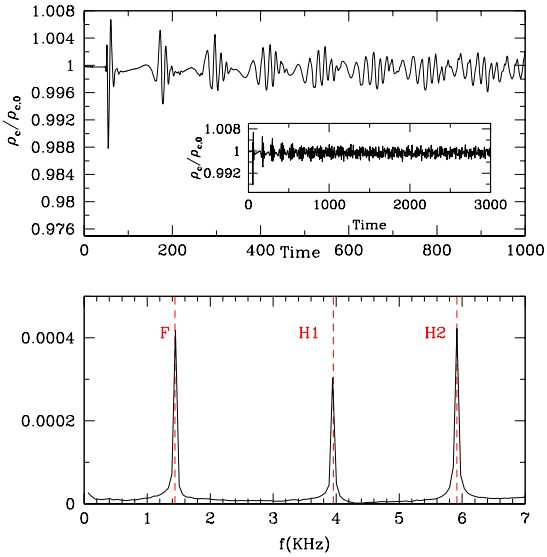

Figure 4. Time evolution of the normalized central density for an $M = 1.4$, $\kappa = 100$, $N = 1$ polytrope. Power spectrum of the evolution of the central rest-mass density is shown in the bottom panel. F, H1 and H2 represent the frequency of the fundamental mode and the first two overtones computed by [23].

panel of Fig. 4 we plot the time evolution of the central rest-mass density for a simulation with $\Delta r = 0.025$ and $N_r = 4000$ until $t = 1000$. In the inset we show the same quantity for the whole evolution. We observe that the truncation errors at this resolution are enough to excite small periodic radial oscillations, visible in this plot as periodic variations of the central density. We see that the damping of the periodic oscillations of the central rest-mass density is very small during the whole evolution, which highlights the low numerical viscosity of the implemented scheme.

By computing the Fourier transform of the time evolution of the central rest-mass density we obtain the power spectrum, which is shown with a solid line in the bottom panel of Fig. 4, while the dashed vertical lines indicate the fundamental frequency and the first two overtones computed by [23]. Note that the locations of the frequency peaks for the fundamental mode and the two overtones are in very good agreement, the relative error in the fundamental frequencies being less than 0.1%. The result of this simulation shows the ability of the scheme to maintain the numerical stability in long-term non-vacuum regular spacetime simulations in spherical coordinates without the need of an additional regularization at the origin.

5.4. Gravitational collapse of a marginally stable spherical relativistic star

We next test the capability of the code to follow BH formation with the gravitational collapse to a BH of a marginally stable spherical relativistic star. For this test, we consider a $\kappa = 100$, $N = 1$ polytropic star with central rest-mass density $\rho_c = 3.15 \times 10^{-3}$, so that its gravitational mass is $M = 1.64$ and its baryon rest-mass $M_* = 1.79$. In order to induce the collapse of the star, we initially increase the rest-mass density by 0.5%.

We present numerical results for a simulation of the gravitational collapse of a marginally

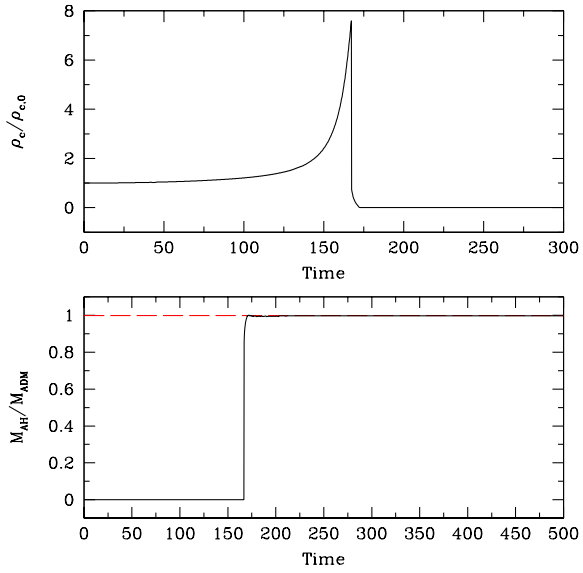

Figure 5. Time evolution of the normalized central density (top) and mass of the AH in units of the ADM mass of the system (bottom) for the collapse of a marginally stable spherical star to a BH.

stable spherical relativistic star performed with resolution of $\Delta r = 0.125$. We use the gauge conditions given in (12)–(14). We plot, in Fig. 5, the time evolution of the normalized central density until $t = 300$ (top), and of the mass of the AH in units of the ADM mass of the system until $t = 500$ when we stopped the simulation (bottom). Overall, as the collapse proceeds the star increases its compactness, reflected in the increase of the central density as shown in the top panel. The most unambiguous signature of the formation of a BH during the simulation is the formation of an AH. Once an AH is found by the AH finder, we monitor the evolution of the AH area, and also of its mass which is plotted, in the bottom panel of Fig. 5. This panel shows that approximately at $t \sim 167$, an AH is first found and that the mass of the AH relaxes to the ADM mass of the system. The difference in the ADM mass and the mass of the AH at $t = 500$, is about 0.2%. Results of this simulation indicate that the numerical scheme to integrate the evolution equations in time can handle accurately the transition between a regular spacetime (that of the star) and a irregular spacetime containing a puncture singularity at $r = 0$.

6. Summary

We have reviewed the work of Montero & Cordero-Carrión [12] who presented results from a numerical code solving the BSSN equations in spherical symmetry and the general relativistic hydrodynamic equations written in flux-conservative form. Montero & Cordero-Carrión [12] applied a second-order PIRK method to integrate in time the evolution equations in curvilinear coordinates, and produced the first successful numerical simulations of vacuum and non-vacuum spacetimes using the covariant BSSN formulation in spherical coordinates without the need for a regularization algorithm at the origin. We have discussed this approach and showed a number of tests to assess the accuracy and expected convergence of the code, namely a pure gauge wave, the evolution of a single BH, the evolution of a spherical relativistic star in equilibrium, and the gravitational collapse of a spherical relativistic star leading to the formation of a BH. Finally, we refer to [24] for details on the implementation of this approach to the BSSN equations in

spherical polar coordinates without any symmetry assumptions in three spatial dimensions.

Acknowledgments
P.M. acknowledges support by the Deutsche Forschungsgesellschaft (DFG) through its Transregional Centers SFB/TR 7 "Gravitational Wave Astronomy". I. C.-C. acknowledges support from Alexander von Humboldt Foundation and AYA2010-21097-C03-01 of the Spanish MICINN.

References

[1] Nakamura T, Oohara K and Kojima Y 1987 *Prog. Theor. Phys. Suppl.* **90** 1
[2] Shibata M and Nakamura T 1995 *Phys. Rev. D* **52** 5428
[3] Baumgarte T W and Shapiro S L 1999 *Phys. Rev. D* **59** 024007
[4] Brown J D 2009 *Phys. Rev. D* **79** 1004029
[5] Rinne O and Stewart J M 2005 *Class. Quant. Grav.* **22** 1143
[6] Alcubierre M and González J A 2005 *Comp. Phys. Comm.* **167** 76
[7] Ruiz M, Alcubierre M and Nuñez D 2008 *Gen. Rel. Grav.* **40** 159
[8] Alcubierre M and Mendez M D 2011 *Gen. Rel. Grav.* **43** 2769
[9] Cordero-Carrión I and Cerdá-Durán P 2012 *Preprint arXiv:1211.5930 [math-ph].*
[10] Cordero-Carrión I, Cerdá-Durán and Ibáñez J M 2012 *Phys. Rev. D* **85** 044023
[11] Bonazzola S, Gourgoulhon E, Grandclément P and Novak J 2004 *Phys. Rev. D* **70** 104007
[12] Montero P J, and Cordero-Carrión I 2012 *Phys. Rev. D* **85** 124037
[13] Bona C, Massó J, Seidel E and Stela J 1997 *Phys. Rev. D* **56** 3405
[14] Alcubierre M, Brügmann B, Diener P, Koppitz M, Pollney D, Seidel E and Takahashi R 2003 *Phys. Rev. D* **67** 084023
[15] Banyuls F, Font J A, Ibánez J M, Martí J M and Miralles J A 1997 Astrophys. J. **476** 221
[16] Gottlieb S and Shu C W 1998 *Math. Compt.* **67** 73
[17] Kreiss H O and Oliger J 1973 *Methods for the Approximate Solution of the Time Dependent Problems*, edited by GARP Publ. Ser.
[18] Harten A, Lax P D and van Leer B 1983 *SIAM Rev.* **25** 35
[19] Einfeldt B 1988 *SIAM J. Numer. Anal.* **25** 294
[20] Hannam M, Husa S, Pollney D, Brgmann B and OMurchadha N 2007 *Phys. Rev. Lett.* **99** 241102
[21] Hannam M, Husa S, Brügmann B, Gonzlez J A, Sperhake U and OMurchadha N 2007 *J. Phys. Conf. Ser.* **66** 012047
[22] Font J A, Stergioulas N and Kokkotas K D 2000 *MNRAS* **313** 678
[23] Font J A, Goodale T, Iyer S, Miller M, Rezzolla L, Seidel E, Stergioulas N, Suen W M and Tobias M 2002 *Phys. Rev. D* **65** 084024
[24] Baumgarte T W, Montero P J, Cordero-Carrión I and Müller E 2013 *Phys. Rev. D* **87** 044026